HIGH-ORDER CURVILINEAR SIMULATIONS OF FLOWS AROUND NON-CARTESIAN BODIES

OLIVIER MARSDEN[*], CHRISTOPHE BOGEY[†] and CHRISTOPHE BAILLY[‡]

Laboratoire de Mécanique des Fluides et d'Acoustique
Ecole Centrale de Lyon & UMR CNRS 5509
69134 Ecully, France
[*]Olivier.Marsden@ec-lyon.fr
[†]Christophe.Bogey@ec-lyon.fr
[‡]Christophe.Bailly@ec-lyon.fr

The current work describes the application of high-order numerical techniques to single or multiple overset curvilinear body-fitted grids, demonstrating the feasibility of direct computations of noise radiated by flows around complex non-Cartesian bodies. Flows of both physical and industrial interest can be investigated with this approach. We first rapidly describe the numerical techniques implemented in our curvilinear simulations. The explicit high-order differencing and filtering schemes are presented, as well as their application to the curvilinear Navier–Stokes equations. We then present brief results of various 2-D acoustic simulations. First the flow around a cylinder, and the associated acoustic field, are described. The diameter-based Reynolds number $Re_D = 150$ is under the critical Reynolds number of the onset of 3-D phenomena in the vortex-shedding. Simulation results can thus be meaningfully compared to experimental measurements. A case of acoustic scattering is then examined. A non-compact monopolar source is placed half way between two differently sized cylinders. A complex diffraction pattern is created, and resulting RMS pressure data are compared to the analytical solution. Finally the noise generated by a low Reynolds number laminar flow around a NACA 0012 airfoil is presented.

Keywords: Direct noise computation; high-order; curvilinear; acoustic scattering; aerodynamic noise.

1. Introduction

The development, over the past twenty years, of high-fidelity numerical methods, has opened whole new perspectives in the domain of numerical simulations. Indeed such methods have allowed the simultaneous pursuit of two highly desirable and slightly contradictory goals, that of lowering error in terms of dispersion and dissipation, and that of reducing the necessary number of discretization points per wavelength.

It has thus become possible to simulate complex phenomena with high and quantified accuracy. This is of particular interest in the field of Computational Aeroacoustics (CAA), where several orders of magnitude separate the energy and wavelengths of propagative acoustic fluctuations from those of the flow features, and where large propagation distances are often encountered. The demands on the accuracy of the numerical schemes as well as on their capacity to cope with a small number of points per wavelength are therefore particularly stringent.

Both explicit schemes, such as Tam and Webb's DRP scheme[1] or those proposed by Bogey and Bailly,[2] and implicit schemes such as Lele's Padé-type,[3,4] have been shown to meet the above criteria and have been successfully applied to aeroacoustic simulations.

High-order schemes typically require large stencils, and are therefore generally implemented on structured grids. Complex curved geometries, while relatively easy to treat thanks to unstructured methods, are often impossible to mesh with a structured Cartesian grid without resorting to extrapolation techniques[5] and their associated problems for the implementation of solid boundary conditions.

This difficulty can be overcome by the use of curvilinear transformations combined with overset multiple grid techniques, often referred to as Chimera techniques.[6] Such methods have sparked considerable interest over the last few years, and recent simulations have shown the feasibility of multiple grid high-fidelity simulations, in the fields of fluid mechanics and electromagnetics, and also more specifically in that of aeroacoustics, for example by Lummer *et al.*[7] who used such methods to examine interactions between a vortex and an airfoil trailing edge.

In this article we focus on aeroacoustic Navier–Stokes simulations, and describe our implementation of explicit high-order methods and overset grid techniques applied on curvilinear grids, as well as present results for three different configurations.

2. Curvilinear Equations

High-order Navier–Stokes simulations having proven their value in the study of noise-generation mechanisms in both free jet flows[8] and rectangular cavity flows,[9] we are developing similar methods for more complex curvilinear geometries.

In this work, the 2-D Navier–Stokes equations are solved on a computational grid which is obtained from the body-fitted grid by applying a suitable curvilinear coordinate transformation. The transformed equations can be written

$$\frac{\partial}{\partial t}\left(\frac{\mathbf{U}}{J}\right) + \frac{\partial}{\partial \xi}\left\{\frac{1}{J}\left[\xi_x(\mathbf{E_e} - \mathbf{E_v}) + \xi_y(\mathbf{F_e} - \mathbf{F_v})\right]\right\}$$
$$+ \frac{\partial}{\partial \eta}\left\{\frac{1}{J}\left[\eta_x(\mathbf{E_e} - \mathbf{E_v}) + \eta_y(\mathbf{F_e} - \mathbf{F_v})\right]\right\} = 0$$

where $\mathbf{U} = (\rho, \rho u, \rho v, \rho e_t)^T$, $J = |\partial(\xi, \eta)/\partial(x, y)|$ is the Jacobian of the geometric transformation between the physical space (x, y) and the computational space (ξ, η), and the fluxes $\mathbf{E_e}, \mathbf{F_e}, \mathbf{E_v}$ and $\mathbf{F_v}$ are given by the following expressions

$$\mathbf{E_e} = \begin{pmatrix} \rho u \\ \rho u^2 + p \\ \rho uv \\ (\rho e_t + p)u \end{pmatrix} \quad \mathbf{E_v} = \begin{pmatrix} 0 \\ \tau_{xx} \\ \tau_{xy} \\ u\tau_{xx} + v\tau_{xy} - q_x \end{pmatrix}$$

$$\mathbf{F_e} = \begin{pmatrix} \rho v \\ \rho uv \\ \rho v^2 + p \\ (\rho e_t + p)v \end{pmatrix} \quad \mathbf{F_v} = \begin{pmatrix} 0 \\ \tau_{xy} \\ \tau_{yy} \\ u\tau_{xy} + v\tau_{yy} - q_y \end{pmatrix}.$$

In the above equations, ρ refers to the fluid density, u and v to the velocity components in the x and y directions, and p to the pressure. Taking into account the perfect gas law, the total specific energy e_t is given by $e_t = p/[(\gamma - 1)\rho] + (u^2 + v^2)/2$. The heat term $\mathbf{q}$ is given by Fourier's law $\mathbf{q} = -(\mu c_p/\sigma)\nabla T$ where $\sigma = 0.72$ is Prandtl's number, μ the molecular dynamic viscosity and c_p the specific heat at constant pressure. The components of the stress tensor $\boldsymbol{\tau}$ are those of a viscous Newtonian fluid.

3. Numerical Aspects

3.1. *Differencing, filtering and time integration techniques, boundary conditions*

A body-fitted grid is first created around the object of interest. Grid construction is performed with care, in order to obtain grid lines of maximal regularity.

Spatial differencing in the interior part of the computational grid is performed with a fourth-order eleven-point explicit centered finite-difference formulation, optimized in the wavenumber space for perturbations of more than 4 points per wavelength, thus ensuring very low dispersion and zero dissipation. Information on the properties of the differencing formulations as well as on the optimization parameters can be found in Bogey & Bailly.[2] The partial derivatives of the transformation's Jacobian matrix are also calculated with the above scheme, using the expression

$$J_{i,j} = \frac{(-1)^{i+j} J_{j,i}^{-1}}{|J^{-1}|}$$

for a 2-D transformation. Care must be taken to ensure that metric identities ensuring the commutative properties of partial differentials are respected.[10,11] Close to solid boundaries, differencing is performed with lower-order stencils, first with the centered 7-point DRP[1] stencil and then with classical centered and finally non-centered 5-point fourth-order stencils. A no-slip solid-wall boundary condition is applied by imposing $u = v = 0$ at the boundary, and also $\partial p/\partial n = 0$ thanks to a one-sided 5-point fourth-order stencil.

Time integration is performed with an explicit 6-stage Runge–Kutta algorithm developed by Bogey *et al.*[2] It is optimized in the wavenumber space, to minimize both dispersion and dissipation for angular frequencies up to $\omega\Delta t = \pi/2$, and is implemented in low-storage form. Stability is guaranteed up to angular frequencies verifying $\omega\Delta t \leq 1.25 \times \pi$.

The very low dissipation exhibited by the numerical algorithm means that high-frequency numerical instabilities of various origins are not naturally damped over time. In this work, these unwanted oscillations are eliminated with a low-pass filter. The main desired property for the filter is high selectivity. To this end, an eleven-point explicit optimized filter[2] is used on the interior of the transformed domain every few time steps. The relative dissipation of the filter is inferior to 5×10^{-3} up to four points per wavelength, and rapidly increases to one for grid-to-grid oscillations. The frequency of the filter application depends on the smoothness or quality of the computational grid, and varies in the simulations presented here from every time step for the airfoil to every five time steps for the

cylinder flow. The frequent application of the filter to the simulated variables allows the use of a small filtering amplitude, typically inferior to 0.1 inside the computational domain.

Close to boundaries, the centered high-order filters described above cannot be used. Unfortunately, boundary conditions tend to generate spurious high-frequency oscillations, rendering some form of filtering necessary. Previously, lower-order centered filters were used, inducing higher dissipation and dispersion close to solid boundaries. To alleviate this problem, the non-centered 11-point highly selective filters designed by Berland *et al.*[12] were adopted, allowing the preservation of high-quality filtering at the boundaries. More information on these filters, as well as the individual filter coefficients, can be found in the above paper.

3.2. *Overset grid techniques*

The use of curvilinear body-fitted grids is often not sufficient to allow high-fidelity simulations around complex objects. The development of multiple overset curvilinear grid techniques is therefore of great interest regarding the generalization of complex aeroacoustic simulations, especially when multiple bodies are involved. With this approach, each object or in some cases each part of an object, is first surrounded by a structured body-fitted grid. The grids either overlap each other sufficiently to ensure that the whole physical domain is covered, or are embedded in an underlying Cartesian grid that spans the entire area of interest. During the simulation, the boundary points in the overlapping zones are updated by interpolating their values from those of the donor grid.

The quality of the interpolation depends essentially on the precise knowledge of the receiving point coordinates with respect to the donor grid, and on the chosen interpolation method. Generally, donor and receiver points are not coincident, so the receiver point coordinates with respect to the donor grid are not known *per se*. They must be calculated with care, especially when high-order interpolation is subsequently used. The interpolation method adopted here is described for a 2-D application, but can be generalized to three dimensions. Indeed, the interpolated value at a receiving point P is obtained thanks to a total of $N+1$ successive interpolations on the donor grid, as shown on Fig. 1 for a 2-D case, where N is the stencil size of the interpolation scheme.

First, interpolation is carried out in the η direction with the P_η coordinate, to calculate the values at the N intersection points of the line $\mathcal{D}$ with the η grid lines. The value at the point P is then interpolated from the N values previously calculated, with the P_ξ coordinate. In order to speed up the overall interpolation process, coordinates of the receiver point projected on the donor grid, as well as those of the N intersection points are calculated at the end of the grid generation phase and stored for quick retrieval during the simulation. Nevertheless, the current implementation of 2-D interpolation remains computationally expensive and slow.

Different single-dimension interpolation techniques have been examined, and in particular cubic splines and Lagrange polynomial functions of varying orders. Figure 2 show a comparison between four interpolating functions: Lagrange polynomials on eleven and
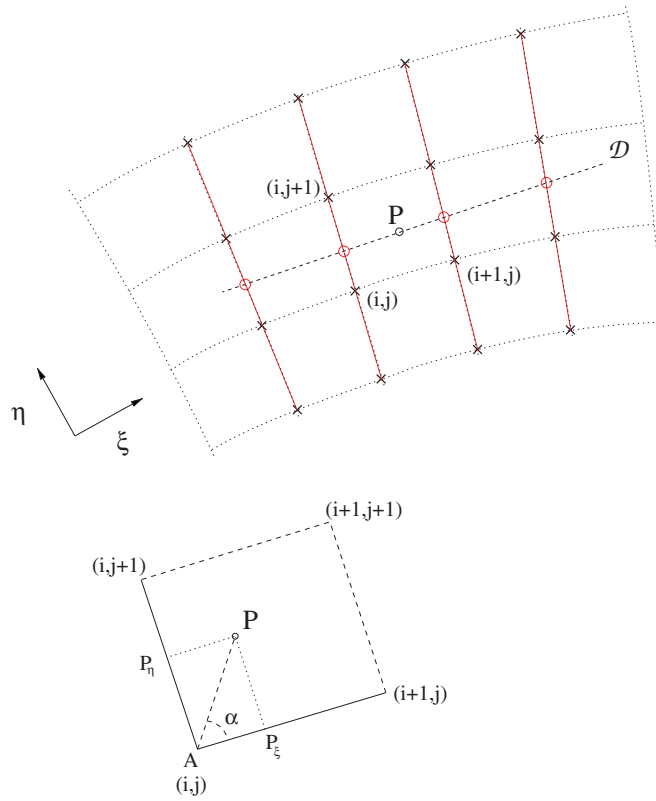
Fig. 1. 2-D interpolation method, shown for $N = 4$. Coordinates P_ξ and P_η of the receiving point P with respect to the underlying donor grid are used to perform successive 1-D interpolations parallel to ξ and η grid lines.
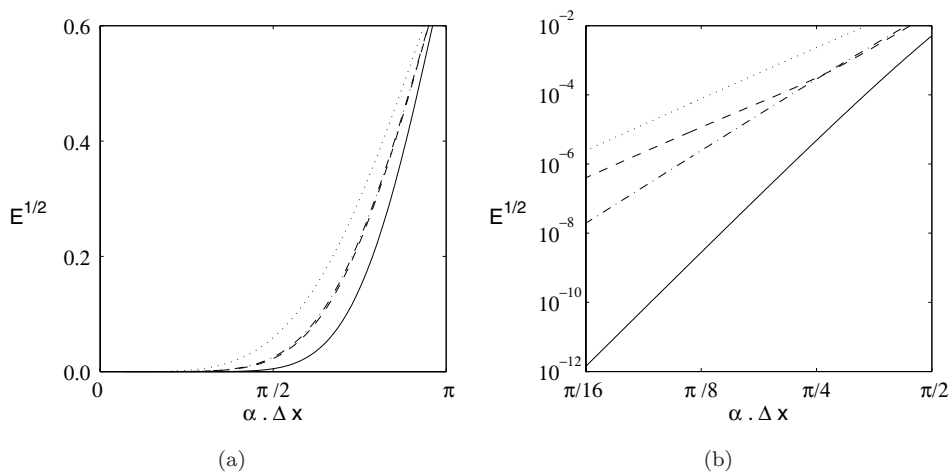

Fig. 2. Interpolation error comparison. $\cdots\cdots$ four-point spline, $---$ six-point spline, $-\cdot-\cdot-$ seven-point Lagrange polynomials, $\longrightarrow$ eleven-point Lagrange polynomials.

seven points, and spline functions on six and four points. The local error function for the wavenumber $\alpha = 2\pi/\lambda$ corresponding to the wavelength λ is defined by

$$E^{1/2}(\alpha) = \left(\int_0^\lambda \left(\hat{f}_\alpha(\delta x) - f_\alpha(\delta x) \right)^2 \delta x \right)^{\frac{1}{2}}$$

where $\hat{f}_\alpha(x)$ represents the interpolated value of f_α at point x, and $f_\alpha(x) = \sin(\alpha x)$. While the interpolation error certainly diminishes with the interpolation order, it is interesting to note that the six-point spline outperforms the seven-point Lagrange polynomial for wavenumbers verifying $\alpha \Delta x > 0.85$, i.e. for waves discretized by less than 7.4 points per wavelength.

The precision required of the interpolation depends on the simulation being carried out. For example in acoustic scattering simulations such as the two-cylinder diffraction problem described later in this work, the interpolation process at the grid interface is applied directly to acoustic fluctuations, and therefore the error on the radiated pressure can be estimated directly from the accuracy of the method. On the other hand, in cases where inhomogenous flow crosses the interpolation interface, relatively small interpolation errors on the velocity components can lead to unacceptably large modifications in the radiated pressure field. In the two-cylinder diffraction test-case presented later, six-point spline interpolation was chosen as a good compromise between accuracy and computational cost.

4. Test Cases

4.1. *Cylinder at a Reynolds number of 150*

The first test case is that of the flow around a cylinder. As the current simulation code is 2-D, a very low Reynolds number $\text{Re}_D = U_\infty D/\nu$ of 150, where D is the cylinder diameter, was chosen in order to remain below the onset of three-dimensional behavior in the wake, which appears between Reynolds numbers of 160 to 180.[13] This should enable a reasonable comparison between experimental flow results and the present numerical simulation.

The upstream Mach number of the flow around the cylinder is $\text{M}_\infty = 0.33$, and the cylinder diameter $D = 2 \times 10^{-5}$ m. The radial step at the cylinder wall is $D \times 0.01$, and the grid dimensions are 300 points in the radial direction by 500 points in the azimuthal direction. A ten-point overlap in the wake region is used to impose a periodic condition in the azimuthal direction. The five points of overlap at each azimuthal extremity of the computational grid thus allow the use of the eleven-point differencing and filtering schemes around the entire grid circumference.

Flow characteristics are compared to those given by previous numerical and experimental studies of low-Reynolds-number cylinder flows. The Strouhal number, which characterizes the frequency of the von Kármán vortex street behind the cylinder, is found to be 0.184, in agreement with values of the literature as is shown in Fig. 3. The mean drag coefficient C_D of 1.32, illustrated in Fig. 4, shows good agreement with both experimental data[13,15] and recent numerical studies.[14,16,17] Likewise, the RMS lift coefficient C_L' of 0.37 compares
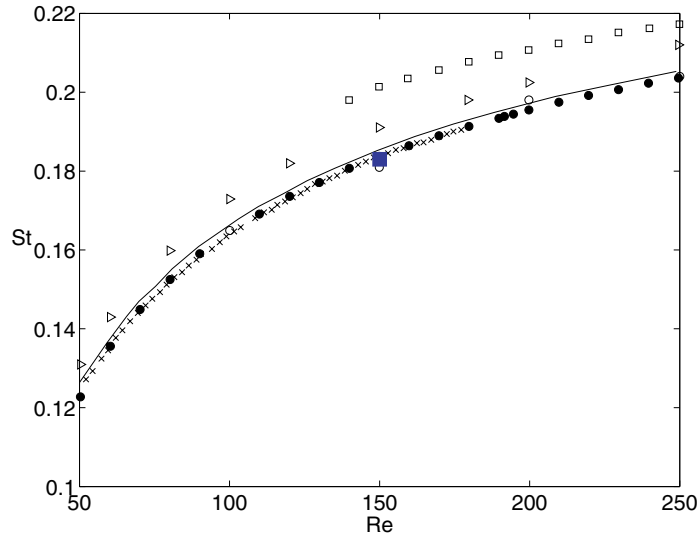
Fig. 3. Comparison of our calculated Strouhal number with various experimental and numerical studies from Posdziech and Grundmann.[14] ▷ Zhang *et al* (1995), □ Thompson *et al* (1996), --- Henderson (1997), ○ Persillon and Braza (1998), ● Posdziech and Grundmann (2001), ■: present simulation.
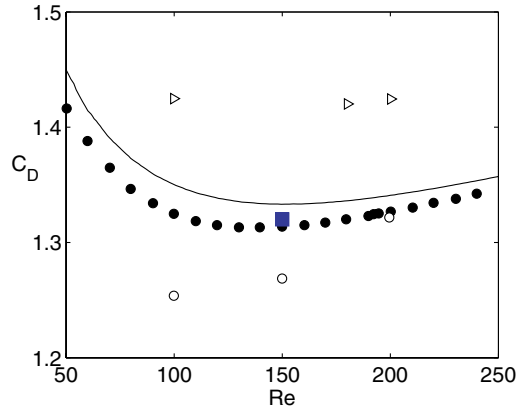

Fig. 4. Evolution of the drag coefficient with the Reynolds number. ---: Henderson (1995), ▷: Zhang *et al.* (1995), ○: Persillon and Braza (1998), ●: Posdziech and Grundmann (2001), ■: current work.

favorably with numerical simulations performed by both Zhang *et al.*[13] and Kravchenko *et al.*[17] Finally, velocity profiles in the cylinder wake compare very well over a large downstream distance to those given by an autosimilar analytical solution for a plane wake, as illustrated in Fig. 5. The physics of the cylinder flow and in particular the effective Reynolds number[18] thus appear to be correctly captured by the present simulation.

Thanks to the high precision and low dissipation of the numerical scheme, the radiated pressure waves are preserved over the entire computational domain, as it can be seen in Fig. 6. The acoustic radiation is almost perfectly dipolar, with a negligible quadrupolar
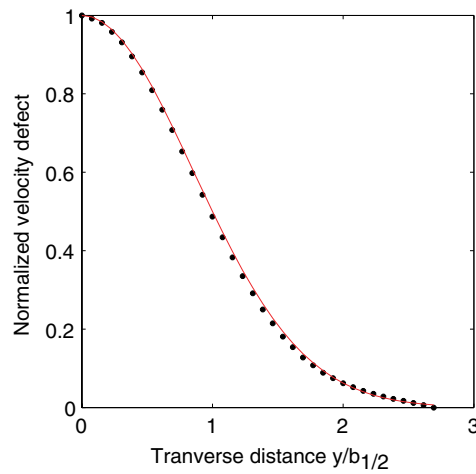
Fig. 5. Mean velocity profile in the cylinder wake region. Velocity deficit versus transversal distance. — 2-D analytical autosimilar solution[19] • Simulated values.
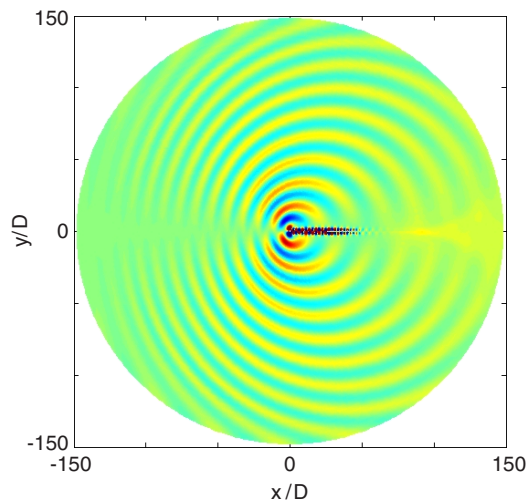

Fig. 6. Instantaneous pressure field around a cylinder at a Reynolds number of 150 and Mach number of $M_\infty = 0.33$. Distance is rendered nondimensional by the cylinder diameter D. Pressure color scale is between -200 and $200\,\mathrm{Pa}$.

contribution, as expected for a low-Mach number cylinder flow.[20] Our radiation levels have not been verified, due to the lack of experimental acoustic results at this low Reynolds number.

The theory of vortex sound applied to the æolian tone problem by Crighton[21] and Howe[22] suggests that the dipolar acoustic radiation is created by the diffraction of quadrupolar aerodynamic sources in the near-cylinder wake. With this view in mind, Figs. 7, 8 and 9 represent the evolution over one period T_p of the near-cylinder vorticity field, pressure field
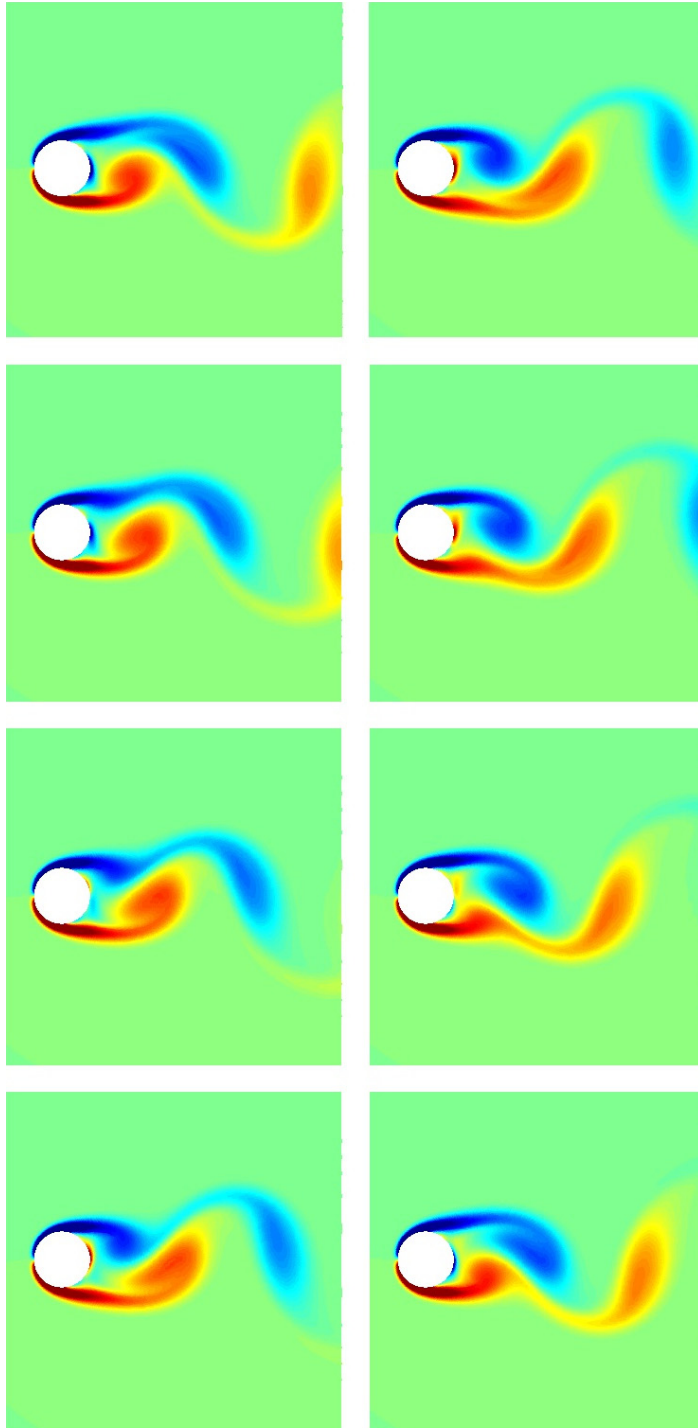
Fig. 7. Vorticity around the cylinder plotted over one period of the vortex shedding. Color scale is between -3×10^7 and 3×10^7, and the domain shown spans $-D$ to $5D$ in the x direction and $-3D$ to $3D$ in the y direction. The time-step between two snapshots is $T_p/8$.
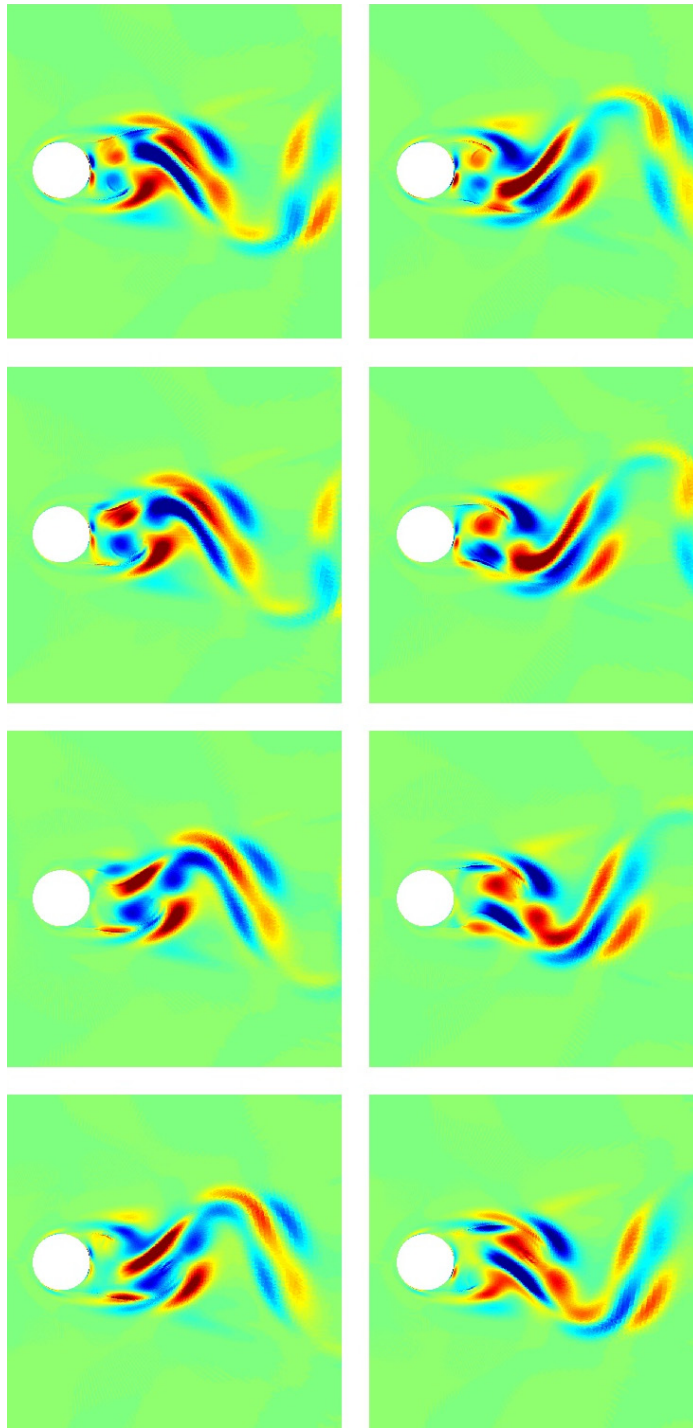
Fig. 8. Source term $S = \nabla \cdot (\rho \boldsymbol{\omega}' \times \mathbf{v}')$, plotted over one period of the vortex shedding. Domain shown spans $-D$ to $5D$ in the x direction and $-3D$ to $3D$ in the y direction. The time-step between two snapshots is $T_p/8$.
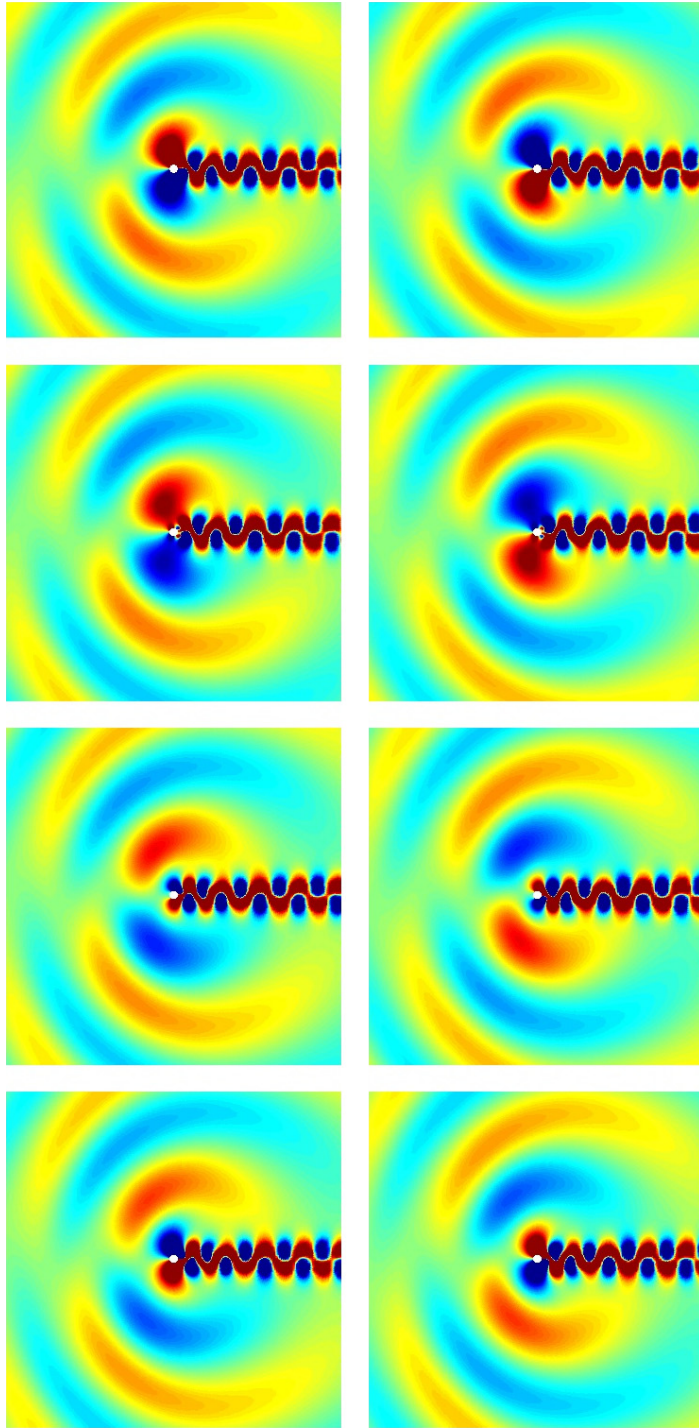
Fig. 9. Fluctuating pressure around the cylinder plotted over one period of the vortex shedding. Color scale is between -1000 and 1000 Pa, and the domain shown spans $-20D$ to $20D$ in both x and y directions. The time-step between two snapshots is $T_p/8$.

and a source term proposed by Powell[23] and defined by

$$S = \rho_\infty \nabla \cdot (\boldsymbol{\omega}' \times \mathbf{v}')$$

where $\boldsymbol{\omega}' = \boldsymbol{\omega} - \bar{\boldsymbol{\omega}}$ is the fluctuating vorticity and $\mathbf{v}' = \mathbf{v} - \bar{\mathbf{v}}$ is the fluctuating speed. It should be noted that only the nonlinear part of the original formulation is represented here. A distribution of quadrupolar nature can be seen in the cylinder wake, centered roughly one cylinder diameter downstream from the cylinder surface. The intensity of S farther downstream in the cylinder wake diminishes rapidly.

4.2. *Diffraction by two cylinders*

The second test-case presented here is the diffraction of sound by two circular cylinders of different diameters, as presented in the proceedings of the 4th CAA workshop.[24] All distances are rendered nondimensional by the larger cylinder's diameter D. The smaller cylinder's diameter is half that of the larger, and the separation between the two cylinders is $8D$. The sound source is a noncompact monopole located half-way between the two cylinders, whose expression is given by

$$S = \sin(\omega t) \, \exp\left(-\ln 2 \, \frac{x^2 + y^2}{b^2}\right)$$

where $b = 0.2$ is the Gaussian half-width of the source and $\omega = 8\pi$ its angular frequency with a time-scale of D/c_∞. A highly complex pressure diffraction pattern is generated by this configuration, providing a challenging test for the curvilinear solver. Indeed, the amplitude of the diffracted field is only around 10^{-5} for a source of amplitude 1. It should also be noted that the test-case difficulty is greatly dependent on the equations being solved. When solving the nonlinearized Euler equations, the acoustic fluctuations must be calculated around a mean value, for instance 10^5 for the pressure, whereas for the linearized Euler equations the fluctuations are directly computed. This test-case is therefore a severe challenge for our nonlinearized solver.

Figure 10 shows a snapshot of the instantaneous pressure field around the two cylinders. The overset grid approach presented above was used to perform the simulation. A circular grid was built around each cylinder, with a central zone where both grids overlap, as shown on Fig. 11. Grid sizes were 700 points in the azimuthal direction by respectively 360 and 400 points in the radial direction for the larger and smaller cylinder. This corresponded to a spatial discretization of eight points per wavelength on average, with tighter spacing close to the cylinders. The interpolation zones thus created contained roughly 5700 points for each grid. Simulation time was of the order of 2.5 h per 1000 iterations on a 2GHz Intel Xeon processor, one period of the monopolar source requiring 140 iterations. The RMS results presented underneath were calculated over 5 periods, after an initial 140 periods of simulation, corresponding roughly to 20 000 iterations.

The different interpolation functions mentioned in Sec. 3.2 were examined. Four-point spline interpolation yielded poor results, resulting in overly low and slightly displaced RMS pressure maxima. Six-point splines and seven-point Lagrange polynomials both
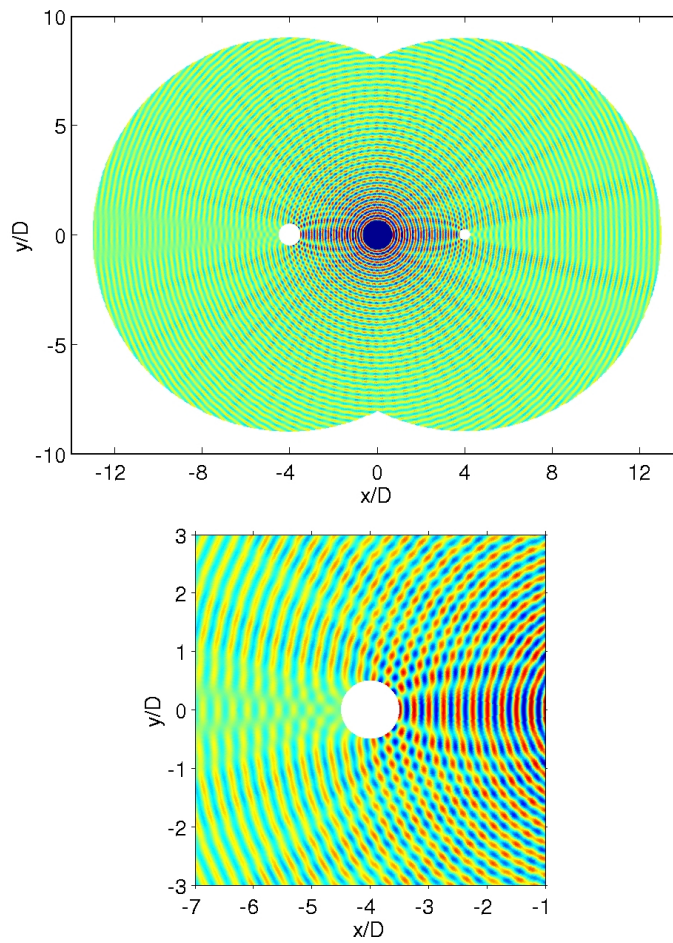
Fig. 10. Two cylinder diffraction problem. Snapshot of the fluctuating pressure field over the entire compu-
tational domain, and a closer view of the pressure field around the larger left cylinder. Pressure color scale
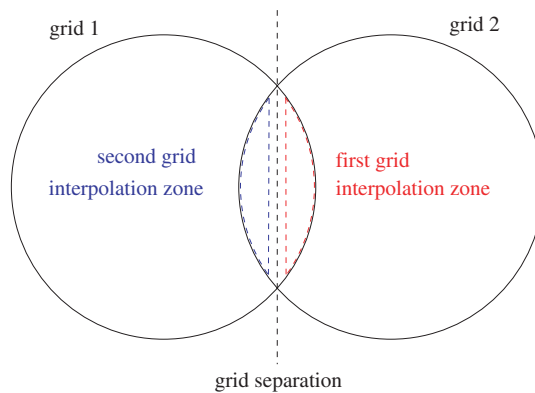is between -10^{-6} and 10^{-6} Pa.

Fig. 11. Grid construction for two-cylinder diffraction. A circular grid is built around each cylinder, and the
resulting overlap zone is used to allow communication between the two grids.
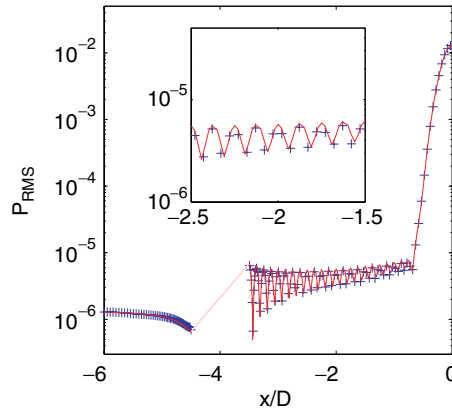
Fig. 12. RMS pressure on the horizontal axis between the two cylinders. — analytical solution by Sherer,[25] + simulated values.

showed very similar results, considerably better than those obtained with four-point spline interpolation. However, errors of slightly less than 5% remain on the calculated RMS pressure field. The RMS pressure values along the horizontal $y = 0$ axis obtained with six-point spline interpolation are plotted in Fig. 12, and compared to the analytical solution by Sherer.[25]

Additional simulations were subsequently performed with eleven-point Lagrange polynomials, to ascertain the origin of the remaining errors. A simulation with interpolation based on eleven-point Lagrange polynomials was undertaken on an identical grid, and yielded identical results, indicating that the residual errors in the spline simulation were not due to the choice of spline interpolation. Another simulation with the same spline interpolation and with smaller mesh sizes yielded improved results. Having checked that this improvement was not linked to the inner-domain numerical scheme, it was deduced that the calculation of the interpolation point coordinates with respect to the donor grid was in large part responsible for the remaining discrepancies in the calculated RMS data. The current coordinate calculation relies on bilinear interpolation, so in the future we will examine the benefits of using bicubic interpolation, which should already substantially reduce coordinate calculation imprecisions.

4.3. *Noise generated by an airfoil in a laminar flow*

Finally we show an example of the calculation of the noise radiated by a NACA 0012 airfoil in a laminar flow. The airfoil chord c measures $8\,\mathrm{mm}$ and the radial step at the boundary wall is $5 \times 10^{-4}c$. The structured computational grid is composed of 1000 points in the azimuthal direction and 200 in the radial direction, and is of C-type,[26] with an overlap in the wake zone allowing the implementation of a periodic condition between the top and bottom halves of the grid. Careful attention was paid to grid construction to minimize oscillations in the Jacobian matrix coefficients. Indeed it is well known that high-order difference schemes inevitably generate high-frequency oscillations when they are
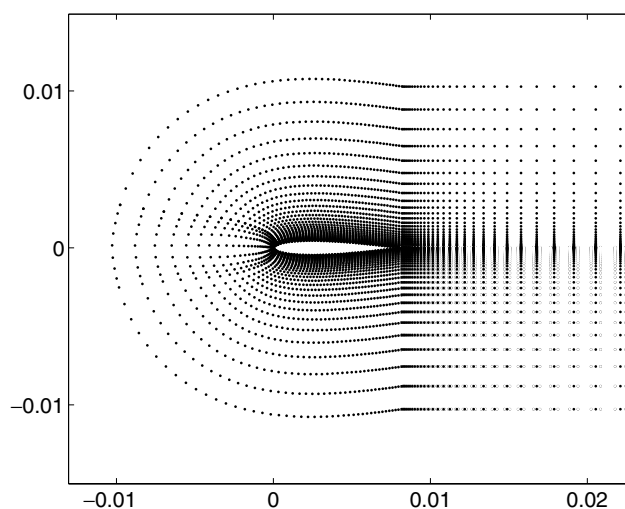
Fig. 13. Central grid around a NACA 0012 airfoil.

applied to sudden discontinuities.[11,27] The trailing edge is a particularly sensitive grid zone since such discontinuities for terms such as $\partial \xi / \partial x$ cannot be avoided with resorting to a relatively costly interpolation technique. To minimize problems in the vicinity of the trailing edge, radial (η) grid lines are not perpendicular to the airfoil boundary, which allows us to impose a continuous variation for three of the four terms in the Jacobian matrix. Only $\partial \eta / \partial x$ remains necessarily problematic. Grid smoothing is performed, to reduce differences in size between upstream mesh elements, which are large because of the very small radius of curvature at the airfoil leading edge, and the considerably smaller downstream mesh elements. The explicit high-order spatial filtering removes the remaining spurious high-frequency oscillations generated by the discontinuous fourth Jacobian term. Figure 13 shows the central portion of the final grid around the airfoil.

We have limited our simulations to relatively low Reynolds numbers. The chord-based Reynolds number of the simulation presented here is around $\mathrm{Re}_c = 60\,000$, at a Mach number of $\mathrm{M}_\infty = 0.33$. This low Reynolds number generates a steady and regular flow structure around the airfoil, with a von Kármán-like vortex street in the wake zone. As expected, the resulting acoustic radiation is strongly dipolar, with a marked upstream directivity. Figure 14 presents a snapshot of the instantaneous fluctuating pressure field around the airfoil.

5. Conclusions and Future Developments

A high-fidelity curvilinear solver with multiple overset grid capability has been shown to give good results for various 2-D aeroacoustic simulations, both with and without flow. The simulated flow around a cylinder at a very low Reynolds number is in good agreement with experimental and numerical studies, and acoustic radiation is preserved over the entire
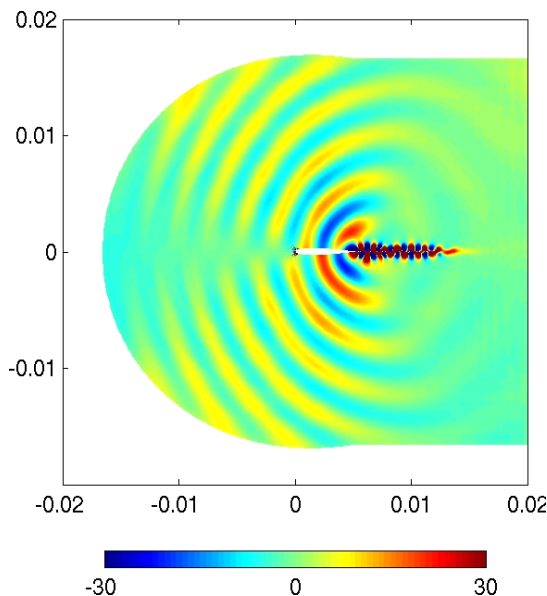
Fig. 14. Fluctuating pressure field around a NACA 0012 airfoil at $\mathrm{Re}_c = 60\,000$ and $\mathrm{M}_\infty = 0.33$. Pressure color scale is between -30 and $30\,\mathrm{Pa}$.

computational domain. Acoustic scattering by a two-cylinder layout compares favorably with analytical results. Finally a low-Reynolds-number flow around an airfoil is presented.

Numerical resolution is performed with eleven-point explicit optimized finite-difference schemes and low-pass filters, combined with an explicit six-step low-storage optimized Runge–Kutta algorithm. Non-centered high-order filters are used near computational boundaries. Different interpolation methods have been implemented and tested for the overset grid communication process, with six-point spline showing promising results. The acoustic scattering simulation showed the importance of accurately calculating the coordinates of receiving grid points with respect to the donor grid. To this end, bicubic interpolation will be tested for the coordinate point calculation.

Future developments include a 3-D curvilinear compressible LES solver to allow the realistic simulation of complex high-Reynolds-number flows. The solver will maintain the general structure of the current code based on the resolution of the curvilinear Navier–Stokes equations with high-order explicit spatial and temporal schemes, and will rely on overset grid techniques to allow the examination of flows around multiple bodies of complex geometries.

Acknowledgment

References

1. C. K. W. Tam and J. C. Webb, Dispersion-relation-preserving finite difference schemes for computational acoustics, *J. Comput. Phys.* **107** (1993) 262–281.
2. C. Bogey and C. Bailly, A family of low dispersive and low dissipative explicit schemes for noise computations, *J. Comput. Phys.* **194**(1) (2004) 194–214.
3. S. K. Lele, Compact finite difference schemes with spectral-like resolution, *J. Comput. Phys.* **103** (1992) 16–42.
4. M. Visbal and D. Gaitonde, High-order-accurate methods for complex unsteady subsonic flows, *AIAA J.* **37**(10) (1999) 1231–1239.
5. K. A. Kurbatskii and C. K. W. Tam, Cartesian boundary treatment of curved walls for high-order computational aeroacoustics schemes, *AIAA J.* **35**(1) (1997) 133–140.
6. J. A. Benek, J. L. Steger, F. C. Dougherty and P. G. Buning, Chimera: A Grid-Embedding Technique, *AEDC-TR-85-64* (1986).
7. M. Lummer, J. W. Delfs and T. Lauke, Simulation of sound generation by vortices passing the trailing edge of airfoils, *AIAA Paper 2002-2578* (2002).
8. C. Bogey, C. Bailly and D. Juvé, Noise investigation of a high subsonic, moderate Reynolds number jet using a compressible LES, *Theoretical and Computational Fluid Dynamics* **16**(4) (2003) 273–297.
9. X. Gloerfelt, C. Bailly and D. Juvé, Direct computation of the noise radiated by a subsonic cavity flow and application of integral methods, *J. Sound Vib.* **266**(1) (2003) 119–146.
10. P. D. Thomas and C. K. Lombard, The Geometric conservation law — a link between finite-difference and finite-volume methods of flow computation on moving grids, *AIAA J.* **17**(10) (1978) 1030–1037.
11. M. Visbal and D. Gaitonde, On the use of higher-order finite-difference schemes on curvilinear and deforming meshes, *J. Comput. Phys.* **181** (2002) 155–185.
12. J. Berland, C. Bogey and C. Bailly, Optimized explicit schemes: Matching and boundary schemes, and 4th-order Runge-Kutta algorithm, *AIAA Paper 2004-2814* (2004).
13. H. Zhang, U. Fey, B. R. Noack, M. Knig and H. Eckelmann, On the transition of the cylinder wake, *Phys. Fluids* **7**(4) (1995) 779–794.
14. O. Posdziech and R. Grundmann, Numerical simulation of the flow around an infinitely long circular cylinder in the transition regime, *Theoret. Comput. Fluid Dynamics* **15**(2) (2001) 121–141.
15. C. H. K. Williamson, Oblique and parallel modes of vortex shedding in the wake of a circular cylinder at low Reynolds numbers, *J. Fluid Mech.* **206** (1989) 579–627.
16. A. Persillon and M. Braza, Physical analysis of the transition to turbulence in the wake of a circular cylinder by three-dimensional Navier–Stokes simulation, *J. Fluid Mech.* **365** (1998) 23–88.
17. A. G. Kravchenko, P. Moin and K. Shariff, B-spline method and zonal grids for simulations of complex turbulent flows, *J. Comput. Phys.* **151** (1999) 757–789.
18. C. Bogey and C. Bailly, Decrease of the effective Reynolds number with eddy-viscosity subgrid-scale modeling, *AIAA J.* **43**(2) (2005) 437–439.
19. C. Bailly and G. Comte-Bellot, *Turbulence* (CNRS éditions, Paris, France, 2003).
20. X. Gloerfelt, F. Pérot, C. Bailly and D. Juvé, Flow-induced cylinder noise formulated as a diffraction problem for low Mach numbers, *J. Sound Vib.* (2005), to appear.
21. D. G. Crighton, Basic principles of aerodynamic sound generation, *Prog. Aerospace Sci.* **16**(1) (1975) 31–96.
22. M. S. Howe, *Acoustics of Fluid-Structures Interactions* (Cambridge University Press, 1998).
23. A. Powell, Theory of vortex sound, *J. Acoust. Soc. Am.* **36** (1964) 177–195.

24. S. Sherer and M. Visbal, Computational study of acoustic scattering from multiple bodies using a high-order overset grid approach, *AIAA Paper 2003-3203* (2003).
25. S. E. Sherer, Scattering of sound from axisy — metric sources by multiple circular cylinders, *J. Acoust. Soc. Am.* **115**(2) (2004) 488–496.
26. J. F. Thomson, B. K. Soni and N. P. Weatherill, *Handbook of Grid Generation* (CRC Press, 1999).
27. R. Vichnevetsky, Propagation through numerical mesh refinement for hyperbolic equations, *Math. Comp. Simulation*, **XXIII** (1981).